

PRISMS. U37126, a very blue, ISM-naked starburst at $z = 10.255$ with nearly 100% Lyman continuum escape fraction

R. Marques-Chaves¹*, J. Álvarez-Márquez², L. Colina², S. Kendrew³, Abdurro'uf⁴, C. Blanco-Prieto², L. A. Boogaard⁵, M. Castellano⁶, K. I. Caputi⁷, A. Crespo-Gomez⁸, A. Fontana⁶, Y. Fudamoto⁹, S. Fujimoto^{10, 11}, M. García-Marín³, Y. Harikane¹², S. Harish⁸, T. Hashimoto^{13, 14}, T. Hsiao¹⁵, E. Iani¹⁶, A. K. Inoue^{17, 18}, D. Langeroodi¹⁹, R. Lin²⁰, J. Melinder²¹, L. Napolitano⁶, G. Östlin²¹, P. G. Pérez-González², C. Prieto-Jiménez², P. Rinaldi²², B. Rodríguez Del Pino², P. Santini⁶, Y. Sugahara^{17, 18}, A. Varo-O'ferral², G. Wright²³, and J. Zavala²⁰

(Affiliations can be found after the references)

Received ; accepted

ABSTRACT

We present very deep (≈ 11 hours on-source) JWST/MIRI low-resolution spectroscopy of the rest-frame optical emission of U37126, a UV-bright ($M_{\text{UV}} \approx -20$), mildly lensed ($\mu \approx 2.2$) galaxy at $z = 10.255$. The continuum emission is well detected in both NIRSpec and MIRI spectra, yet no nebular recombination or metal emission lines are observed ($EW_0(\text{H}\beta + [\text{O III}]) \leq 300 \text{ \AA}$ and $EW_0(\text{H}\alpha) \leq 400 \text{ \AA}$, at 3σ). Combined with the exceptionally blue UV continuum slope, $\beta_{\text{UV}} \approx -2.9$, and weak/flat Balmer break, these constraints indicate a stellar population dominated by very young and massive stars with a strongly suppressed nebular contribution. Comparisons with synthetic stellar population models indicate that U37126 requires both a very high ionizing photon production efficiency, $\log(\xi_{\text{ion}}/\text{Hz erg}^{-1}) \approx 25.75$, and a nearly unit LyC escape fraction, of $f_{\text{esc}} \geq 86\%$ (3σ) based on $\text{H}\alpha$ flux limit and $f_{\text{esc}} = 0.94 \pm 0.06$ derived independently from SED fitting. The best-fit SED yields a (de-lensed) stellar mass of $M_{\star} \approx 10^{7.8} M_{\odot}$ and a star-formation rate of $\text{SFR} \approx 10 M_{\odot} \text{ yr}^{-1}$ ($\text{sSFR} \sim 160 \text{ Gyr}^{-1}$), that along with its very compact size, $r_{\text{eff}} \approx 61 \text{ pc}$, yields very high stellar mass and star-formation-rate surface densities, $\Sigma_{M_{\star}} \approx 3 \times 10^3 M_{\odot} \text{ pc}^{-2}$ and $\Sigma_{\text{SFR}} \approx 400 M_{\odot} \text{ yr}^{-1} \text{ kpc}^{-2}$. Together with the lack of detectable nebular emission, these properties suggest that U37126 is undergoing an “ISM-naked” starburst phase, possibly driven by an extremely efficient gas-to-star conversion followed by strong feedback that has cleared the remaining gas from its stellar core, allowing most LyC photons to escape. Finally, we show that even a small fraction of galaxies like U37126 ($\approx 3\%-6\%$), with extreme LyC production and escape, could contribute disproportionately ($\approx 50\%-100\%$) to the ionizing photon budget during cosmic reionization.

Key words. Galaxies: starburst – Galaxies: high-redshift – Galaxies: ISM – Cosmology: dark ages, reionization, first stars

1. Introduction

The James Webb Space Telescope (JWST) is fundamentally reshaping our understanding of galaxy formation in the early Universe by enabling the detection and detailed characterization of the first galaxies within the first few hundred million years after the Big Bang (e.g., Castellano et al. 2022; Curtis-Lake et al. 2023; Harikane et al. 2023; Pérez-González et al. 2023; Carniani et al. 2024; Castellano et al. 2024; Harikane et al. 2024; Naidu et al. 2025; Napolitano et al. 2025; Chemerynska et al. 2026). Deep NIRCam imaging and NIRSpec spectroscopy provide unprecedented access to the rest-frame ultraviolet (UV) and optical emission of galaxies at redshifts $z \gtrsim 7$, while MIRI extends such studies to even higher redshifts. Together, JWST observations are now robustly constraining the physical properties of the earliest galaxies that were previously inaccessible, including their stellar populations, star-formation histories, and nebular emission (e.g., Álvarez-Márquez et al. 2024; Bunker et al. 2023; Fujimoto et al. 2024; Álvarez-Márquez et al. 2025; Helton et al. 2025; Roberts-Borsani et al. 2025; Tang et al. 2025; Zavala et al. 2025; Donnan et al. 2026).

The UV continuum slope, β_{UV} ($f_{\lambda} \propto \lambda^{\beta_{\text{UV}}}$), is a widely used spectral diagnostic for the physical conditions in star-forming galaxies. Prior to JWST, observations established that typical star-forming galaxies at $z \gtrsim 2$ exhibit relatively blue UV

slopes ($\beta \approx -2$), and that UV continua become systematically bluer toward higher redshifts and fainter UV luminosities (e.g., Bouwens et al. 2012; Finkelstein et al. 2012; Bouwens et al. 2014; Bhatawdekar & Conselice 2021). These trends are generally interpreted as reflecting lower dust attenuation and younger stellar populations in early galaxies. Recent JWST observations have extended these measurements even above $z > 10$ with improved precision, revealing an increasing prevalence of very steep UV slopes among the earliest galaxies (e.g., Topping et al. 2022; Cullen et al. 2023, 2024; Morales et al. 2024; Saxena et al. 2024; Topping et al. 2024a; Dottorini et al. 2025; Messa et al. 2025).

While moderately blue β_{UV} can be readily produced by hot, massive stars expected in young stellar populations, achieving very steep slopes ($\beta \lesssim -2.6$) is considerably more challenging and requires additional physical conditions. At the young ages ($\lesssim 10 \text{ Myr}$) necessary to generate such intrinsically blue stellar continua, nebular emission powered by ionizing photons typically contributes significantly to the observed spectrum, acting to redden the emergent UV spectrum (e.g., Bouwens et al. 2010). As a result, stellar population models generally predict that UV slopes approaching $\beta \approx -3$ should be rare or unobservable in systems where ionizing photons are efficiently reprocessed by surrounding gas (e.g., Katz et al. 2025). Extremely blue UV slopes thus point to conditions in which the contribution of nebular emission to the emergent UV spectrum is strongly suppressed. This naturally occurs when a significant fraction of

* Rui.MarquesCoelhoChaves@unige.ch

Lyman continuum (LyC, with > 13.6 eV) ionizing photons escape from H II regions before being reprocessed into nebular line and continuum emission.

Galaxies exhibiting extremely steep UV slopes together with weak nebular emission thus represent compelling candidates for systems with exceptionally high LyC escape fractions and enhanced ionizing photon output. This framework was first explored by Zackrisson et al. (2013, 2017) who showed that the combination of steep UV slopes and weak rest-optical emission lines provides a powerful means of identifying strong LyC emitters. This not only has the advantage of selecting sources with very high LyC f_{esc} , but also with exceptionally high ionizing photon production efficiencies, $\xi_{\text{ion}} = Q_{\text{H}}/L_{\text{UV}}$, where Q_{H} is the hydrogen-ionizing photon production rate and L_{UV} is the UV luminosity. Such high ξ_{ion} values are expected in very young stellar populations required to reproduce extremely steep UV continuum slopes.

Nevertheless, and with a few exceptions (Marques-Chaves et al. 2022), confirmed low-redshift LyC emitters exhibit only moderately blue β_{UV} (Chisholm et al. 2022) and generally strong nebular emission lines, with rest-frame H β equivalent widths exceeding > 150 Å (e.g., Izotov et al. 2016, 2018; Flury et al. 2022). Only recently, JWST started to reveal a rare, yet non-negligible population of $z > 6$ sources with both extremely blue UV slopes and weak nebular emission lines (Topping et al. 2022; Hainline et al. 2024; Donnan et al. 2025; Yanagisawa et al. 2025), often with inferred LyC escape fractions well above $f_{\text{esc}} > 50\%$ (e.g., Giovinazzo et al. 2025).

In this work, we present the discovery of another such system, UNCOVER-37126 at $z = 10.255$ (hereafter U37126), previously identified by Atek et al. (2023) and spectroscopically confirmed by Fujimoto et al. (2024). Leveraging ultra-deep JWST/MIRI spectroscopy of its rest-frame optical emission, together with ancillary NIRCam imaging and NIRSpec spectroscopy, we show that U37126 exhibits an extremely steep UV continuum slope and a non-detection of nebular emission lines, consistent with LyC escape fraction close to unity. The paper is organized as follows. Section 2 presents the MIRI, NIRCam, and NIRSpec observations. Section 3 describes the observational results, which are discussed in Section 4. Finally, Section 5 summarizes our conclusions. Throughout this work, we use a concordance cosmology with $\Omega_{\text{m}} = 0.31$, and $H_0 = 67.7 \text{ km s}^{-1} \text{ Mpc}^{-1}$ (Planck Collaboration et al. 2020).

2. JWST Observations and data reduction

U37126 was observed with the Low Resolution Spectrograph (LRS, Kendrew et al. 2015) of the Mid-Infrared Instrument (MIRI, Rieke et al. 2015; Wright et al. 2015, 2023) on 7–8 November 2025 as part of the "PRImordial galaxy Survey with MIRI Spectroscopy at $z \sim 10$ " (PRISMS, program ID 8051; PIs: J. Álvarez-Márquez & L. Colina). These observations provide a spectral coverage between $4.80 - 14.0 \mu\text{m}$ wavelength range using a $0''.51 \times 4''.7$ slit, i.e., from $\lambda_{\text{rest}} \approx 0.43 - 1.20 \mu\text{m}$ in the rest-frame, and a spectral resolution of $R \sim 100$. The total on-source integration time was 39,696 s (≈ 11.0 h), obtained using a customized four-point dither strategy repeated over 12 dithers. The target acquisition was done using the F560W filter on a GAIA DR3 reference star.

The data reduction follows Álvarez-Márquez et al. (in prep.). Briefly, we use version 1.20.2 of the JWST calibration pipeline and CRDS context `jwst_1464.pmap`, following the standard MIRI LRS procedures (Bushouse et al. 2025) with additional

custom steps to optimize background subtraction and artifact removal. These include wavelength masking, master and residual background subtraction, and sigma clipping to mitigate detector artifacts and cosmic-ray residuals. The final combined 2D spectrum and 1D extracted spectrum were produced using the pipeline Stage 3, with the 1D spectrum extracted using a $0''.44$ aperture and corrected for aperture losses using the standard JWST reference files (`jwst_miri_apcorr_0017.fits`). For more details, see Álvarez-Márquez et al. (in prep.).

In addition to the MIRI LRS observations, NIRCam imaging and NIRSpec spectroscopy of U37126 are publicly available as part of the UNCOVER project¹. NIRCam photometry, combining medium- and broad-band filters from F070W to F480M, is taken from the UNCOVER DR3 SUPER catalog (Suess et al. 2024; Weaver et al. 2024). NIRSpec Micro-Shutter Assembly (MSA) spectroscopy, obtained with the low-resolution PRISM ($R \sim 100$), is taken from the UNCOVER data release 4 (Bezanson et al. 2024). We use the fully reduced and calibrated NIRSpec spectrum (≈ 4.4 hours on-source) published by Fujimoto et al. (2024). Finally, we adopt the updated gravitational magnification from the UNCOVER DR4, $\mu = 2.19 \pm 0.05$ (Furtak et al. 2023; Price et al. 2025).

To place all JWST observations of U37126 on a consistent relative flux scale, we first compute synthetic NIRSpec photometry convolving the NIRSpec spectrum with the filter transmission functions of all medium- and broad-band NIRCam filters, where the source is significantly detected ($\geq 3\sigma$; F150W–F480M) and compare it to the corresponding NIRCam photometry. This yields a scaling factor of ≈ 1.41 , which is applied to the NIRSpec spectrum. For the MIRI LRS spectrum, we compute synthetic photometry over the common spectral range $\lambda_{\text{obs}} = 4.85 - 5.30 \mu\text{m}$, where the continuum is significantly detected in both NIRSpec and MIRI. We find consistent flux densities between the two spectra in this region, and therefore apply no additional scaling to the MIRI LRS spectrum. Figure 1 shows the combined NIRSpec and MIRI spectra together with the NIRCam photometry.

3. Results

U37126 was first identified by Atek et al. (2023) as a photometric redshift candidate at $z_{\text{phot}} = 10.60_{-0.31}^{+0.21}$ based on NIRCam photometry (ID: 39074). A spectroscopic redshift of $z_{\text{spec}} = 10.255 \pm 0.001$ was subsequently reported by Fujimoto et al. (2024), based on the unambiguous detection of the Ly α break. A tentative detection of the N III] $\lambda 1750$ emission line was also discussed in Fujimoto et al. (2024); however, we do not find significant emission at the reported wavelength, nor evidence for any other rest-frame UV or optical emission lines in the NIRSpec and MIRI spectra (Fig. 1). We therefore adopt the redshift $z = 10.255 \pm 0.001$ inferred from the Ly α break throughout this work. Finally, U37126 was recently observed in the far-infrared with ALMA; however, neither dust continuum emission nor [O III] $88 \mu\text{m}$ line emission was detected, yielding upper limits of $\log(M_{\text{dust}}/M_{\odot}) < 6.06$ and $L(\text{[O III]} 88 \mu\text{m}) < 2 \times 10^8 L_{\odot}$, respectively (Algera et al. 2025).

3.1. Spectral properties from NIRSpec, NIRCam, and MIRI

The β_{UV} is measured using several independent methods based on both NIRSpec and NIRCam. We first fit the NIRSpec/PRISM spectrum over a broad and continuous rest-frame window,

¹ <https://jwst-uncover.github.io/>

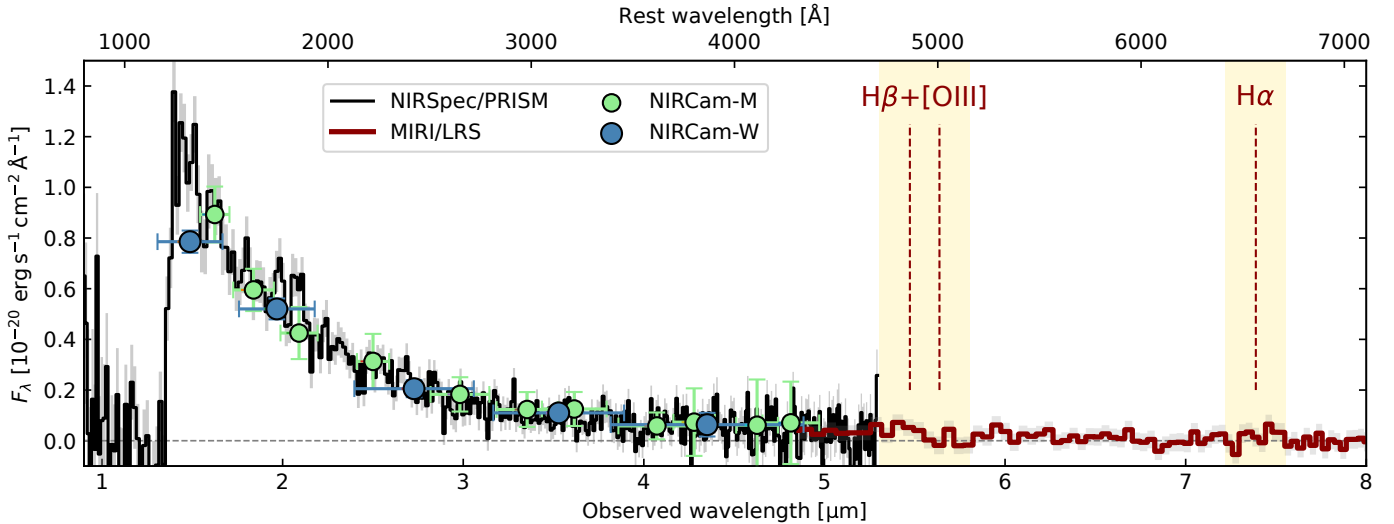


Fig. 1. NIRSpec/PRISM (black) and MIRI/LRS (red) spectra of U37126 with the 1σ uncertainties shown in grey. The expected locations of the main rest-frame optical emission lines, $H\beta$, $[O\text{ III}]\lambda\lambda 4960, 5008$, and $H\alpha$, are indicated with red dashed lines. NIRCam photometry from broad- and medium-band filters is overplotted in blue and green, respectively.

1400 – 3600 Å, thereby excluding regions potentially affected by intergalactic medium (IGM) absorption blueward of 1400 Å and by the Balmer break at longer wavelengths. A power-law fit using `lmfit` (Newville et al. 2025) yields $\beta_{\text{UV}} = -2.79 \pm 0.07$. We then adopt the continuum windows defined by Calzetti et al. (1994), which avoid ISM absorption features, stellar P-Cygni profiles, and nebular emission lines. To remain consistent with the above criteria, we restrict the fit to windows at $\lambda_{\text{rest}} \geq 1400$ Å, obtaining $\beta_{\text{UV}} = -2.83 \pm 0.09$. As an alternative spectral diagnostic, we fit a first-order polynomial to the wavelength intervals 2180 – 2220 Å and 2780 – 2820 Å following Leitherer et al. (1999). This method yields $\beta_{\text{UV}} = -3.05 \pm 0.16$. Finally, we use the NIRCam broad-band photometry in F200W and F277W, which sample the rest-frame range $\lambda_{\text{rest}} \simeq 1800 - 2500$ Å. From this, we obtain $\beta_{\text{UV}} = -2.86 \pm 0.20$. Taken together, these independent diagnostics consistently indicate that U37126 shows a steep UV continuum slope, all with $\beta_{\text{UV}} \lesssim -2.7$. Taking the simple average of these measurements, obtained from different spectral regions and instruments (NIRSpec and NIRCam), and adopting their standard deviation as the uncertainty, we derive a fiducial UV slope of $\beta_{\text{UV}} = -2.88 \pm 0.10$.

Another key spectral diagnostic is the strength of the Balmer break, which is sensitive to the age of the stellar population and to the relative contribution of nebular emission. For consistency and to facilitate a direct comparison with the stellar population models discussed next in Section 3.2, we estimate the Balmer break strength of U37126 from the NIRSpec spectrum as the flux density ratio (in F_ν) between $\lambda_{\text{rest}} = 4200$ Å and $\lambda_{\text{rest}} = 3400$ Å, measured within spectral windows of width $\Delta\lambda_{\text{rest}} = 400$ Å. We find a ratio of $F_\nu^{4200\text{Å}}/F_\nu^{3400\text{Å}} = 0.86 \pm 0.21$. For comparison, using the observed NIRCam photometry in the F356W and F444W filters, which sample the emission shortward and longward of the Balmer break, respectively, we derive a consistent flux density ratio of $F_\nu^{F444W}/F_\nu^{F356W} = 0.88 \pm 0.08$. As discussed further in Section 3.2, the inferred Balmer break strength rules out single-burst stellar populations older than $\gtrsim 6$ Myr, as well as continuous star formation histories with ages $\gtrsim 16$ Myr.

Finally, we analyze the MIRI/LRS spectrum. At the redshift of U37126 ($z = 10.255$), the $H\beta$, $[O\text{ III}]\lambda\lambda 4960, 5008$, and $H\alpha$ emission lines are expected at $\lambda_{\text{obs}} = 5.47$ μm, 5.64 μm, and

7.39 μm, respectively, yet none of them are significantly detected (Fig. 1).² We estimate their flux upper limits by measuring the root mean square (rms) of the spectrum within a rest-frame window of $\Delta\lambda = 300$ Å centered on the expected position of each line (yellow regions in Figure 1), and adopt the MIRI/LRS instrumental resolutions of $R \simeq 49$ and $R \simeq 89$ for $[O\text{ III}]$ and $H\alpha$, respectively (Kendrew et al. 2015). The $[O\text{ III}]$ doublet is expected to be unresolved, and we consider an intrinsic $[O\text{ III}] 5008/4960$ ratio of 2.98 (Osterbrock & Ferland 2006).

Under these assumptions, we derive 3σ limits of $F([O\text{ III}]\lambda 5008) \leq 6.6 \times 10^{-19}$ erg s $^{-1}$ cm $^{-2}$ and $F(H\alpha) \leq 6.9 \times 10^{-19}$ erg s $^{-1}$ cm $^{-2}$. The continuum emission is significantly detected in the MIRI/LRS ranges $\lambda_{\text{obs}} = 4.8 - 5.6$ μm (37.2 ± 4.1 nJy) and $5.85 - 6.73$ μm (26.1 ± 5.3 nJy), while no significant signal is observed at $\lambda_{\text{obs}} \geq 7.0$ μm (≤ 28 nJy at 3σ). We estimate the continuum emission of $[O\text{ III}]\lambda 5008$ and $H\alpha$ from the best-fit SED (Section 3.3), finding continuum flux densities of $\simeq 35.8$ nJy and $\simeq 27.7$ nJy, respectively. These values imply 3σ rest-frame equivalent-width limits under $EW_0([O\text{ III}]\lambda 5008) \leq 174$ Å and $EW_0(H\alpha) \leq 400$ Å. For $H\beta$, we assume case-B recombination with an intrinsic line ratio of $I_{H\alpha}/I_{H\beta} = 2.78$, assuming $T_e = 1.5 \times 10^4$ K and $n_e = 10^3$ cm $^{-3}$ (Luridiana et al. 2015). This yields an upper limit of $F(H\beta) \leq 2.5 \times 10^{-19}$ erg s $^{-1}$ cm $^{-2}$ and $EW_0(H\beta) \leq 65$ Å. We emphasize that the $H\beta$ flux and equivalent-width limits are dependent on the assumed case-B recombination conditions. These measurements are summarized in Table 1

Finally, we briefly examine the spectral region around Ly α . Figure 2 shows the rest-frame Ly α break of U37126 and, for comparison, that of MACS0647-JD (Heintz et al. 2024), a star-forming galaxy at a similar redshift ($z = 10.170$) and with comparable global properties (e.g., stellar mass and star formation rate). MACS0647-JD exhibits a strong damped Ly α absorption feature, corresponding to a neutral hydrogen column density of $N_{\text{HI}} \simeq 2.5 \times 10^{22}$ cm $^{-2}$ (Heintz et al. 2024). In contrast, U37126 shows a very sharp Ly α break, consistent with a negligible H I column density along the line of sight and suggestive of its lo-

² The reduced NIRSpec spectrum (v4) from the Dawn JWST Archive extends up to $\lambda_{\text{obs}} \simeq 5.5$ μm, but $H\beta$ is also not detected.

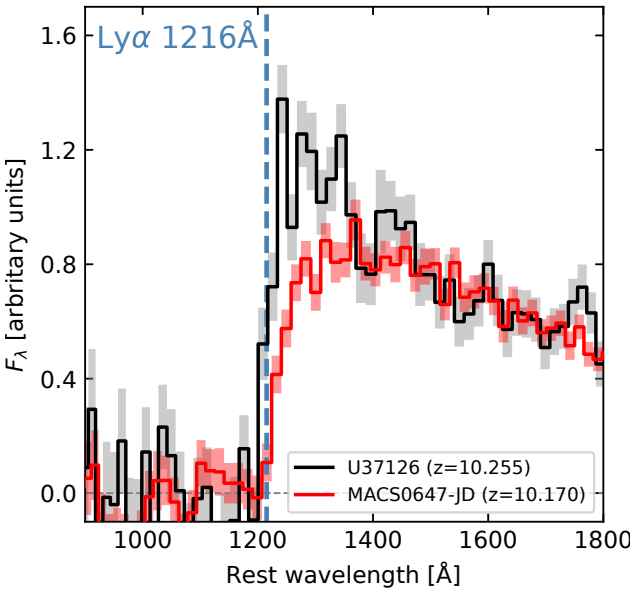


Fig. 2. Comparison of the rest-frame Ly α break of U37126 (black) with that of MACS0647-JD ($z = 10.170$) which shows a strong damped Ly α absorption feature ($N_{\text{HI}} \simeq 2.5 \times 10^{22} \text{ cm}^{-2}$, Heintz et al. 2024).

Table 1. Summary of the properties of U37126. Global quantities have been corrected for lensing magnification.

| Property | Value | Uncertainty |
|--|---------------------------|---------------|
| R.A. [J2000] | 00:14:21.63 | 0.1'' |
| Dec. [J2000] | -30:21:35.10 | 0.1'' |
| z | 10.255 | 0.001 |
| μ | 2.19 | 0.05 |
| M_{UV} [AB] | -20.10 | 0.05 |
| Age [Myr, CSFH] | 6.8 | 1.6 |
| SFR [$M_{\odot} \text{ yr}^{-1}$] | 9.6 | 4.6 |
| $\log(M_{\star}/M_{\odot})$ | 7.77 | 0.06 |
| E(B-V) [mag.] | 0.01 | 0.01 |
| r_{eff} [pc] | 61 | 6 |
| sSFR [Gyr $^{-1}$] | 160 | 80 |
| $\log(\Sigma_{M\star} / M_{\odot} \text{ pc}^{-2})$ | 3.40 | 0.10 |
| $\log(\Sigma_{\text{SFR}} / M_{\odot} \text{ yr}^{-1} \text{ kpc}^{-2})$ | 2.61 | 0.22 |
| β_{UV} | -2.88 | 0.10 |
| EW_0 ([O III] $\lambda 5008 \text{ \AA}$) [\AA] | ≤ 174 | (3 σ) |
| EW_0 (H β) [\AA] | ≤ 64 | (3 σ) |
| EW_0 (H α) [\AA] | ≤ 400 | (3 σ) |
| L ([O III] $\lambda 5008 \text{ \AA}$) [erg s^{-1}] | $\leq 4.3 \times 10^{41}$ | (3 σ) |
| L (H α) [erg s^{-1}] | $\leq 4.5 \times 10^{41}$ | (3 σ) |
| $\log(\xi_{\text{ion}})$ [Hz erg $^{-1}$] | 25.75 | 0.09 |
| f_{esc} (LyC) - H α | ≥ 0.86 | (3 σ) |
| f_{esc} (LyC) - SED | 0.94 | 0.06 |

cation within a large-scale ionized bubble. A more quantitative analysis of the Ly α break profile and the associated constraints on N_{HI} will be presented in forthcoming work.

3.2. Predictions from synthetic stellar models

We now compare the observed spectral properties derived in Section 3.1 with predictions from synthetic stellar population models. We adopt the Binary Population and Spectral Synthe-

sis models (BPASS v2.2.1; Stanway & Eldridge 2018), using their default IMF with slope of -2.35 and an upper mass cutoff of $300 M_{\odot}$ (imf135_300). We assume a metallicity $Z = 0.003$ ($Z/Z_{\odot} \simeq 0.15$ for $Z_{\odot} = 0.02$), consistent with values reported for galaxies of comparable M_{UV} at similar redshifts (e.g., Stiavelli et al. 2023; Boyett et al. 2024; Hsiao et al. 2024; Álvarez-Márquez et al. 2025; Helton et al. 2025). Predictions for additional metallicities are presented in Appendix A and shown in Figure A.1.

We consider both instantaneous-burst and constant star formation histories, with ages from 1 to 100 Myr. For each model, we compute the ionizing photon production rate Q_{H} and predict the associated nebular continuum emission using PyNeb (Luridiana et al. 2015). We assume nebular conditions with $T_e = 1.5 \times 10^4 \text{ K}$ and $n_e = 10^3 \text{ cm}^{-3}$ expected at very high redshifts (e.g., Isobe et al. 2023), and include free-free and free-bound emission by H and He, and the two-photon continuum of H. Hydrogen recombination-line luminosities (e.g., H α) are obtained using the coefficients from Osterbrock & Ferland (2006). We additionally include the contribution of the H γ and H δ emission lines, as these are sampled by the spectral regions used to infer the Balmer break strength ($F_v^{4200 \text{ \AA}}/F_v^{3400 \text{ \AA}}$, see next). The total emergent spectrum is then given by $F_{\text{total}} = F_{\text{stellar}} + (1 - f_{\text{esc}}) \times F_{\text{nebular}}$, where the factor $(1 - f_{\text{esc}})$ accounts for the ionizing escape fraction, i.e., LyC photons not reprocessed into nebular emission. We also assume negligible dust attenuation, given the extremely steep UV slope.

For each model and f_{esc} we measure the UV slope, Balmer-break strength, and EW_0 (H α) using the same methodology applied to U37126 (Section 3.1). Figure 3 (top) shows the predicted quantities as a function of age for $f_{\text{esc}} = 0$, 0.5, and 0.9 (red, green, blue, respectively). Overall, we recover the expected trends already discussed in previous works: increasing f_{esc} suppresses the nebular continuum and line emission, yielding steeper UV slopes and lower EW_0 (H α) at fixed age (e.g., Zackrisson et al. 2013, 2017). UV slopes steeper than $\beta_{\text{UV}} < -2.7$ necessarily require a substantial escape of ionizing photons, and this should hold irrespective of the assumed IMF, metallicity, and age of the underlying stellar population (cf. Katz et al. 2025; Schaerer et al. 2025), and more broadly, for any ionizing source.

The Balmer break, traced here by the flux density ratio $F_v^{4200 \text{ \AA}}/F_v^{3400 \text{ \AA}}$, is close to unit for all burst and constant-SFH models at young ages, reflecting the strong contribution of nebular continuum in the $F_v^{3400 \text{ \AA}}$ but also the emission lines (H γ and H δ) to $F_v^{4200 \text{ \AA}}$, unless f_{esc} is very high (90%, blue). At ages $\gtrsim 6$ Myr ($\gtrsim 15$ Myr) for single burst models (constant star formation), the strength of the Balmer break increases with the stellar age, reflecting the rising contribution of less massive stars (A-type) to the integrated spectrum (e.g., Kuruvanthodi et al. 2024; Loosher et al. 2024; Baker et al. 2025).

The observational constraints for U37126 are overplotted in Fig. 3. These favor stellar populations with very high f_{esc} along with young ages, $\simeq 2 - 10$ Myr for constant star formation or $\simeq 1 - 3$ Myr for single burst models. Thus, our results indicate that the lack of nebular emission in the MIRI/LRS spectrum is primarily driven by an exceptionally high f_{esc} and very young stellar populations, rather than by an evolved population with reduced LyC production. As a simple estimate, we consider a 5 Myr constant-SFH BPASS model redshifted to $z = 10.255$ and scaled to match the observed spectrum. This scaled BPASS model, shown in Figure 4 (violet), has $\log(Q_{\text{H}}/\text{s}^{-1}) \simeq 54.4$ (de-lensed) and a high ionizing photon production efficiency, $\log(\xi_{\text{ion}}/\text{Hz erg}^{-1}) \simeq 25.75$. For comparison, if we use the H α

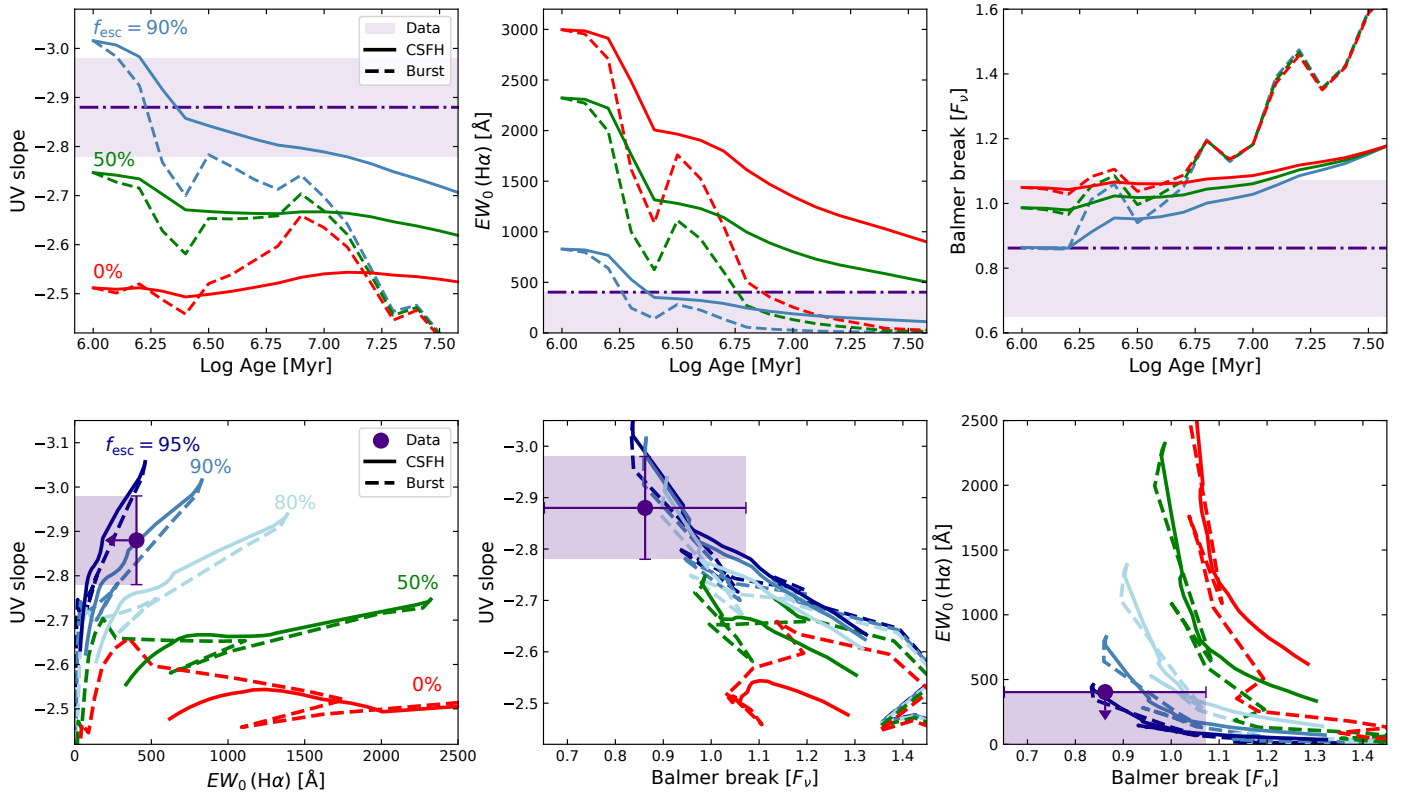


Fig. 3. Predictions from BPASS synthetic stellar and nebular emission models ($Z/Z_{\odot} \simeq 0.15$, $T_e = 1.5 \times 10^4$ K, and $n_e = 10^3$ cm $^{-3}$) for the UV continuum slope (β_{UV}), $EW_0(\text{H}\alpha)$, and the Balmer break strength ($F_v^{4200\text{\AA}}/F_v^{3400\text{\AA}}$) as a function of the age (top) and their combination (bottom). Solid and dashed lines correspond to constant star formation (CSFH) and instantaneous burst models (Burst), respectively. Model sequences are shown for LyC escape fractions f_{esc} ranging from 0% (red) to 90% (blue); additional models with $f_{\text{esc}} = 80\%$ and 95% are shown in the bottom panels only (light and dark blue, respectively). Violet dot-dashed lines (top) and circles (bottom) indicate the observational constraints for U37126, with the shaded regions representing the 1 σ uncertainties, except for $EW_0(\text{H}\alpha)$, which represents the 3 σ upper limit.

limit assuming $f_{\text{esc}} = 0$, we would obtain $\log(\xi_{\text{ion}}/\text{Hz erg}^{-1}) \leq 25.02$ (2 σ), i.e., underpredicting its true ξ_{ion} by > 0.73 dex. Together with our upper limit on the H α luminosity ($L(\text{H}\alpha) \leq 4.5 \times 10^{41}$ erg s $^{-1}$, de-lensed), our results indicate an $f_{\text{esc}} \geq 86\%$ at 3 σ for U37126.

3.3. Spectral energy distribution and global properties

We perform spectral energy distribution (SED) fitting using the SpectroPhotometric version of the CIGALE code (V.2022.1; Burgarella et al. 2005; Boquien et al. 2019; Burgarella et al. 2025), incorporating all NIRCam photometry, the NIRSpec/PRISM spectrum, as well as MIRI/LRS measurements of the [O III] $\lambda 5008$ and H α flux upper limits and the continuum emission between $\lambda_{\text{obs}} = 4.8 - 5.6\text{ }\mu\text{m}$, $5.85 - 6.73\text{ }\mu\text{m}$, and $> 7.0\text{ }\mu\text{m}$ (see Section 3.1). We have excluded from the fit all observations below $\lambda_{\text{rest}} < 1400\text{ \AA}$ since they may be affected by IGM absorption and the effect is not properly handled by CIGALE.

The star formation history (SFH) is modeled assuming constant star formation with ages varying from 1 to 20 Myr in 1 Myr steps. We adopt stellar population models from Bruzual & Charlot (2003), assuming a Chabrier (2003) IMF and metallicities from $Z/Z_{\odot} = 2 - 20\%$. The ionization parameter ranges from $\log(U) = -3.0$ to -1.5 in 0.5 dex steps. We adopt the Milky Way dust extinction law from Cardelli et al. (1989) with $R_V = 3.1$ as the dust attenuation law for the nebular emission and the Calzetti et al. (2000) for the stellar emission. The color excess of the neb-

ular gas is allowed to vary from 0 to 0.5 mag. Finally, the escape of LyC photons is allowed to vary from 0 to 0.999.

Our best-fit SED model ($\chi^2_{\nu} = 0.64$), shown in Figure 4, is characterized by a stellar population with a constant star-formation rate $\text{SFR} = 9.6 \pm 4.6 M_{\odot} \text{ yr}^{-1}$ (10 Myr weighted), a stellar mass $\log(M_{\star}/M_{\odot}) = 7.77 \pm 0.06$, and an age of 6.8 ± 1.6 Myr (where global properties are corrected for magnification, assuming $\mu = 2.19$). This yields a specific star-formation rate $\text{sSFR} = 160 \pm 80 \text{ Gyr}^{-1}$. The color excess is negligible, $E(B-V) = 0.01 \pm 0.01$ mag., as expected given the very steep UV slope of the best-fit model, $\beta_{\text{UV}} = -2.85 \pm 0.05$ (and consistent with our measurements in Section 3.1).

The best-fit model also provides a very high LyC escape fraction, $f_{\text{esc}} = 0.94 \pm 0.06$ (Figure 4, inset panel), consistent with the results obtained in Section 3.2. Finally, using the de-magnified size of $r_{\text{eff}} = 61 \pm 6$ pc derived next in Section 3.4, we obtain a stellar mass and SFR surface densities of $\log(\Sigma_{M_{\star}}/M_{\odot} \text{ pc}^{-2}) = 3.40 \pm 0.10$ and $\log(\Sigma_{\text{SFR}}/M_{\odot} \text{ yr}^{-1} \text{ kpc}^{-2}) = 2.61 \pm 0.22$, respectively. These values are substantially higher than those of typical star-forming galaxies at high- z (e.g., Morishita et al. 2024) and are instead comparable to those found in young massive star clusters and globular clusters (e.g., Vanzella et al. 2023), as well as in some of the most extreme sources at the highest redshifts (Castellano et al. 2022; Tacchella et al. 2023; Naidu et al. 2025). These properties are summarized in Table 1.

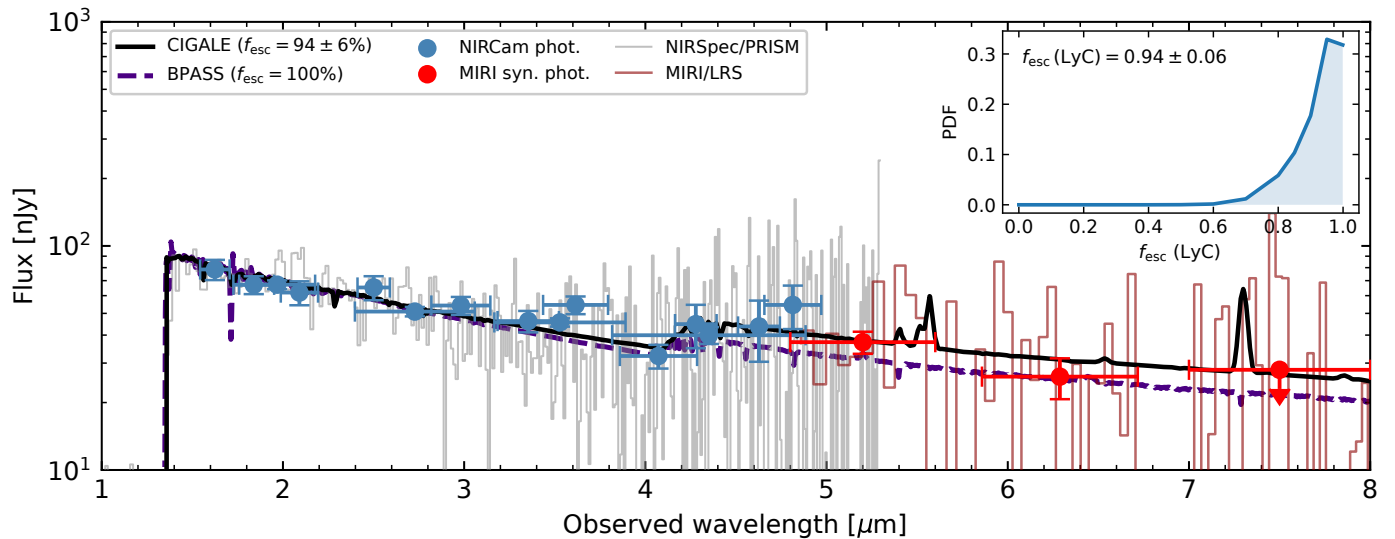


Fig. 4. Best-fit spectral energy distribution (SED) of U37126 derived with CIGALE (black solid curve) and a pure stellar 5 Myr-old BPASS model (CSFH with $Z/Z_{\odot} = 15\%$, violet dashed line). The NIRSpec/PRISM and MIRI/LRS spectra are shown in grey and red, respectively, while NIRCams photometric measurements and MIRI/LRS synthetic photometry are indicated by blue and red circles. The inset panel displays the posterior probability density function of the Lyman-continuum escape fraction.

3.4. Morphology and size

U37126 shows a compact morphology in the NIRCams imaging, as illustrated in the top panels of Fig. 5. To quantify its structural properties, we model the light distribution using PySersic (Pasha & Miller 2023). PySersic performs forward modeling of galaxy morphologies with Sérsic profiles convolved with a supplied point-spread function (PSF), and employs a Bayesian framework to explore the posterior distribution of all parameters and their degeneracies.

Empirical PSFs from the UNCOVER DR4 release (Suess et al. 2024; Weaver et al. 2024) are available for all NIRCams bands, but only at a pixel scale of $0.04''/\text{pix}^{-1}$. Because the short-wavelength NIRCams images (e.g., F150W and F200W) have been resampled in UNCOVER DR4 to a pixel scale of $0.02''/\text{pix}^{-1}$, we generate PSFs for these bands using STPSF³ (Perrin et al. 2014). We follow Morishita et al. (2024) and Weibel et al. (2024) and set the jitter_sigma parameter in WebbPSF to 0.022, which has been shown to best reproduce the observed NIRCams PSFs.

We fit 2D Sérsic models, allowing the Sérsic index to vary between 0.5 and 6.0, while leaving the total flux, effective radius, ellipticity, and position angle free. Given the significantly higher SNR in the NIRCams broadband filters relative to the medium bands, we restrict our morphological analysis to the broadband imaging only, also excluding F444W image for the same reason (low SNR). Each fit is performed on a $1'' \times 1''$ cutout, all centered on U37126.

For the short-wavelength NIRCams images, we measure effective radii of $r_{\text{eff}} = 24 \pm 2$ mas in F150W and $r_{\text{eff}} = 22 \pm 2$ mas in F200W, respectively (Figure 5), and a Sérsic index of $n = 1.64 \pm 0.26$. We adopt the F200W value, as this band probes the rest-frame UV at $\simeq 1750\text{\AA}$. Given that U37126 is moderately magnified by A2744, with $\mu = 2.19 \pm 0.05$ (Furtak et al. 2023; Price et al. 2025), we obtain a de-magnified radius of $r_{\text{eff}} = 61 \pm 6$ pc at $z = 10.255$. At longer wavelengths, the best-fit models yield $r_{\text{eff}} \lesssim 0.5 \text{ pix}$ (or $r_{\text{eff}} \lesssim 0.02''$). Thus, U37126

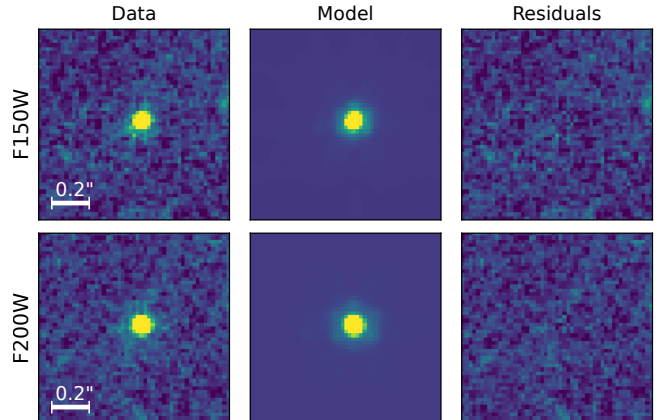


Fig. 5. NIRCams F150W (top) and F200W (bottom) $1'' \times 1''$ cutouts of U37126. Middle and right panels show the Sérsic best-fit models obtained with PySersic and the corresponding residuals, respectively.

appears unresolved in the rest-optical with $r_{\text{eff}} < 160$ pc (or < 100 pc after lensing correction).

4. Discussion

4.1. Comparison with other strong confirmed LyC emitters and $z > 6$ candidates

Our results strongly support a scenario in which U37126 both produces and leaks large amounts of LyC photons. These constraints are driven by the combination of its extremely steep UV continuum and the non-detection of nebular emission, and indirectly, from the very sharp Ly α break. Although extreme, similar properties have been identified with JWST in a small number of sources at $z \sim 6 - 10$ (Topping et al. 2022; Hainline et al. 2024; Giovinazzo et al. 2025; Yanagisawa et al. 2025; Jecmen et al. 2026). These galaxies share comparably blue UV continua and unusually weak nebular emission, pointing toward very young stellar populations with very high LyC f_{esc} . Interestingly, several of these also show high SFRs within extremely compact morphologies ($r_{\text{eff}} < 260$ pc). This results in very high Σ_{SFR} , com-

³ <https://stpsf.readthedocs.io/en/latest/>

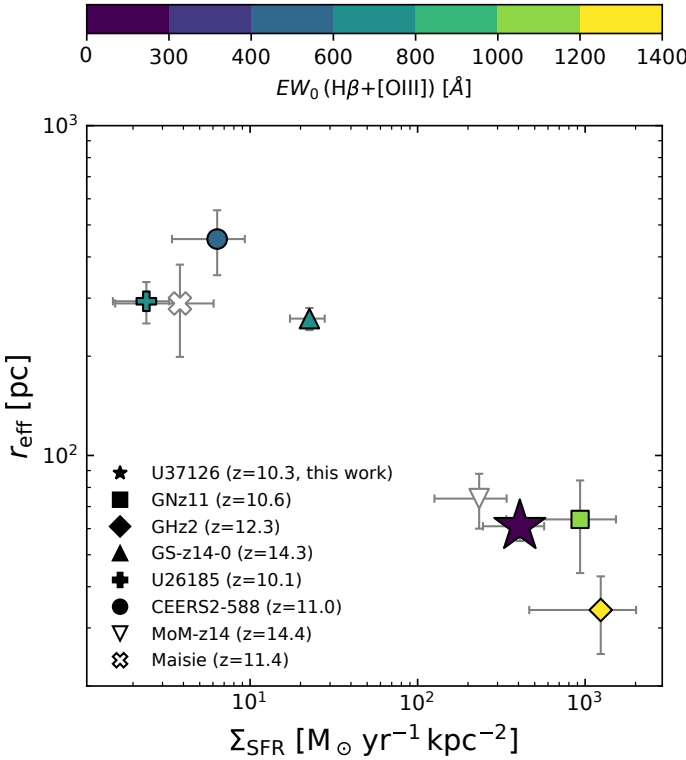


Fig. 6. Effective radius (r_{eff}) as a function of star-formation rate surface density (Σ_{SFR}) for galaxies at $z > 10$ with MIRI constraints on $EW_0(\text{H}\beta + [\text{O III}])$ (color-coded, from: [Castellano et al. 2022](#); [Goulding et al. 2023](#); [Tacchella et al. 2023](#); [Calabro et al. 2024](#); [Carniani et al. 2024](#); [Álvarez-Márquez et al. 2025](#); [Helton et al. 2025](#); [Zavala et al. 2025](#); [Harikane et al. 2026](#), and Alvarez-Marquez et al. in prep.). Symbols denote individual sources while the open symbols indicate sources without available EW_0 measurements ([Arrabal Haro et al. 2023](#); [Naidu et al. 2025](#)). U37126 (star) occupies the compact, high- Σ_{SFR} regime but shows unusually weak nebular emission with $EW_0(\text{H}\beta + [\text{O III}]) < 296 \text{ \AA}$ (3σ) compared to other compact systems (e.g., GNz11 and GHz2), consistent with a high LyC escape fraction.

parable to that inferred for U37126, $\log(\Sigma_{\text{SFR}}/\text{M}_\odot \text{ yr}^{-1} \text{ kpc}^{-2}) \simeq 2.6$, and consistent with expectations for strong LyC leakage ([Sharma et al. 2017](#); [Naidu et al. 2020](#)).

Recent JWST studies have further suggested a dichotomy among galaxies at $z \gtrsim 10$ ([Harikane et al. 2025](#); [Roberts-Borsani et al. 2025](#)), separating extended systems with relatively weak emission lines, in some cases accompanied by Balmer breaks ([Álvarez-Marquez et al. in prep.](#); [Harikane et al. 2026](#)), that may be undergoing a recent decline in star formation (e.g., [Helton et al. 2025](#)), from very compact galaxies ($r_{\text{eff}} \lesssim 100 \text{ pc}$) experiencing recent bursts and exhibiting strong UV and/or optical emission lines (e.g., [Bunker et al. 2023](#); [Castellano et al. 2024](#); [Álvarez-Márquez et al. 2025](#); [Zavala et al. 2025](#)). Figure 6 shows the effective radius and star-formation rate surface density of the small sample of $z > 10$ sources with MIRI constraints on rest-optical emission, with the color scale encoding the rest-frame equivalent width $EW_0(\text{H}\beta + [\text{O III}])$. Compact systems generally occupy the regime of high Σ_{SFR} and large equivalent widths. U37126 lies in this compact, high- Σ_{SFR} regime, yet it shows unusually weak nebular emission, which is naturally explained by its very high LyC escape fraction.

To further place U37126 in context, we compare its observed properties with those of confirmed LyC emitters at lower red-

shifts ($z < 4$), where LyC escape can be measured directly. We first note that the majority of known LyC emitters exhibit relatively modest escape fractions and UV slopes $\beta_{\text{UV}} > -2.5$ (e.g., [Izotov et al. 2018](#); [Steidel et al. 2018](#); [Marques-Chaves et al. 2021](#); [Flury et al. 2022](#); [Kerutt et al. 2024](#)). Only a small subset shows $f_{\text{esc}} > 50\%$ and nearly all of these exhibit strong nebular emission, with typical $\text{H}\beta$ equivalent widths of the order of $\sim 100 - 300 \text{ \AA}$ ([de Barros et al. 2016](#); [Izotov et al. 2016](#); [Vanzella et al. 2016](#); [Izotov et al. 2018](#); [Rivera-Thorsen et al. 2019](#); [Flury et al. 2022](#)). An exception is the strong LyC leaker J1316+2614 at $z = 3.6$, which, despite of being much brighter, has a measured $f_{\text{esc}} \simeq 87\%$, $EW_0(\text{H}\beta) \simeq 35 \text{ \AA}$, and $\beta_{\text{UV}} \simeq -2.6$ ([Marques-Chaves et al. 2022](#)), representing the closest known analog to U37126 and to other $z > 6$ strong LyC emitting candidates with steep UV slopes and weak nebular emission.

At face value, the observed high f_{esc} and strong nebular emission in some confirmed strong LyC emitters appear at odds with the predictions and with the properties of U37126 (Fig. 3). However, these observations are not necessarily contradictory. The measured f_{esc} in low- z LyC emitters probes LyC escape along the line of sight toward the young stars, whereas nebular emission traces a more global, 4π -averaged escape fraction. Strongly anisotropic LyC leakage can therefore result in high apparent f_{esc} values while still producing prominent nebular emission (e.g., [Flury et al. 2022](#); [Jaskot et al. 2024a](#)). In addition, LyC flux measurements close to the Lyman limit may be boosted by nebular bound-free emission ([Inoue 2010](#); [Simmonds et al. 2024b](#)), potentially leading to an overestimation of the stellar f_{esc} . As recently shown by [Izotov et al. \(2025\)](#), this effect appears to be significant in J1243+4646, the strongest LyC emitter at $z \simeq 0.3$ and also a strong line emitter ($f_{\text{esc}} \simeq 72\%$ and $EW_0(\text{H}\beta) \simeq 221 \text{ \AA}$, [Izotov et al. 2018](#)).

These results thus suggest that sources like U37126, characterized by very steep UV slopes with faint nebular emission, may be rare or absent at $z < 4$. However, it remains unclear whether this reflects a genuinely low number density at lower redshifts, possibly due to the specific physical conditions required to form such systems (see Section 4.2), or whether they have been systematically overlooked in LyC surveys due to selection effects (e.g., [Bergvall et al. 2013](#)), as the confirmation of spectroscopic redshifts generally relies on strong nebular emission.

4.2. Conditions for forming “ISM-naked” starbursts with nearly unity LyC escape fraction

The nature of sources like U37126 is intriguing, as typical starburst galaxies are gas-rich and exhibit strong nebular emission. The stringent 3σ upper limits on the equivalent widths, together with the very steep UV continuum and a weak/flat Balmer break strength, indicate that nebular emission is intrinsically weak and at most a small fraction of LyC photons is being reprocessed by surrounding gas.

To obtain a rough estimate of the characteristic size of the ionized region associated with U37126, we compute the Strömgren radius,

$$R_S = \left(\frac{3 Q_H}{4\pi \alpha_B n_H^2} \right)^{1/3},$$

where $Q_H \approx 10^{54.4} \text{ s}^{-1}$ (Section 3), n_H is the hydrogen number density of the surrounding gas, and α_B is the case-B recombination coefficient. For typical electron temperatures $T_e \simeq (1-2) \times 10^4 \text{ K}$ and gas densities $n_H \simeq 10^2 - 10^3 \text{ cm}^{-3}$, we infer Strömgren radii of $R_S \approx 50 - 200 \text{ pc}$. These scales are comparable to,

or exceed, the size of the stellar emission ($r_{\text{eff}} \approx 61$ pc; Section 3.4). Under such extreme conditions, any substantial gas reservoir located within or around U37126 would be expected to be efficiently ionized and, therefore, most likely detectable in the NIRSpec and MIRI spectra.

One possible exception is a scenario in which the ionized gas is extremely diffuse, since line luminosities scale as $L \propto n_e^2$. Even if all LyC photons were fully reprocessed within H II regions, the non-detection of H α emission could, in principle, be explained by an extremely low electron density ($n_e \lesssim 10^{-2} \text{ cm}^{-3}$). However, such conditions are rarely observed and are particularly unlikely for U37126 ($z = 10.255$), given the expected increase of electron density toward higher redshifts (e.g., Isobe et al. 2023). Moreover, the extreme stellar mass and SFR surface densities of U37126 would instead favor high electron densities (e.g., Reddy et al. 2023a,b). Consistent with this expectation, nearly all sources at $z > 10$ with sizes comparable to that of U37126 ($r_{\text{eff}} \approx 61$ pc) exhibit evidence for extremely high gas densities (Harikane et al. 2025), several of them shown in the bottom right corner of Figure 6 (e.g., GNz11, GHz2). Taken together, the absence of detectable nebular emission in U37126 suggests that the galaxy is largely depleted of its interstellar medium. U37126 thus behaves as an ISM-free starburst, raising the question of how such conditions can be achieved.

One possibility is that, during its intense star-formation episode, the bulk of the natal gas in U37126 was rapidly and efficiently converted into stars, leaving little residual gas available to absorb and reprocess LyC photons. Dekel et al. (2023) (see also Li et al. 2023) predict that extremely high gas surface densities ($\Sigma_{\text{gas}} \gtrsim 3 \times 10^5 M_{\odot} \text{ pc}^{-2}$) can lead to the formation of “feedback-free starbursts” (FFB), in which gas clouds collapse on very short free-fall timescales (~ 1 Myr). This makes star formation very efficient, since the cloud collapse occurs before the onset of mechanical feedback (e.g., SNe). While the gas surface density of U37126 cannot be measured directly, the observed stellar mass surface density, $\log(\Sigma_{M\star}/M_{\odot} \text{ pc}^{-2}) = 3.40 \pm 0.10$, suggests a pre-star-formation gas surface density of at least comparable magnitude, thus satisfying the condition for an FFB. Observationally, high star-formation efficiencies have been inferred ($> 40\%$; Dessauges-Zavadsky et al. 2025) and predicted ($> 70\%$; Marques-Chaves et al. 2024) to explain the strong LyC escape directly measured in the strong leaker J1316+2614 at $z = 3.6$ with $f_{\text{esc}} \approx 87\%$ and $EW_0(\text{H}\beta) \approx 35 \text{ \AA}$ (Marques-Chaves et al. 2022).

An alternative, though not mutually exclusive, scenario is that strong feedback has removed gas and dust from the stellar core of U37126, and potentially to larger distances.⁴ In this context, Ferrara et al. (2023) proposed that radiation pressure on dust and gas can drive powerful radiative feedback during super-Eddington phases. Such conditions are expected in the early stages of a starburst, when the sSFR exceeds a critical threshold of $\gtrsim 25 \text{ Gyr}^{-1}$ (Fiore et al. 2023), which is satisfied in this source ($\approx 160 \text{ Gyr}^{-1}$). These phases may also facilitate substantial LyC leakage, as shown recently by Ferrara et al. (2025). Furthermore, recent hydrodynamic simulations have shown that strong radiative outflows can only be efficiently launched in very dense systems with high star-formation efficiencies, leading simultaneously to strong LyC leakage (Menon et al. 2025). Observational evidence for such extreme outflows has been reported in a hand-

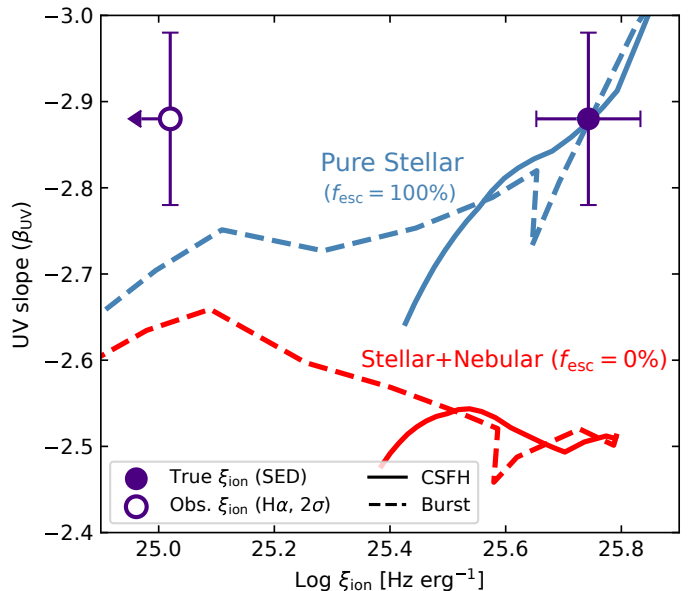


Fig. 7. Relationship between the UV slope (β_{UV}) and the ionizing photon production efficiency (ξ_{ion}) for stellar population synthesis models with (red) and without (blue) the contribution of nebular emission, i.e., representing the extreme cases of $f_{\text{esc}} = 0$ and $f_{\text{esc}} = 1$, respectively. Filled and open circles indicate ξ_{ion} derived from SED fitting and from the H α flux limit assuming $f_{\text{esc}} = 0$, respectively.

ful of powerful starbursts with elevated sSFR (Crespo Gómez et al. 2025; Marques-Chaves et al. 2025), including in confirmed low- z LyC emitters (e.g., Komarova et al. 2025). However, these systems still exhibit intense nebular emission, unlike U37126.

In summary, the absence of detectable gas in U37126 may reflect an evolutionary sequence in which exceptionally efficient star formation rapidly consumes the natal gas, followed by intense feedback that expels the remaining material, including dust, from the stellar core. In the absence of subsequent gas accretion, U37126 may then evolve rapidly into a post-starburst or recently quenched system, like the ones recently identified by JWST at high- z (e.g., Loosher et al. 2024).

4.3. Implications for cosmic reionization

The discovery of powerful ionizing sources such as U37126 has important implications for cosmic reionization. The ionizing photon budget is commonly expressed through the comoving ionizing emissivity, \dot{n}_{ion} , defined as $\dot{n}_{\text{ion}} = \rho_{\text{UV}} \xi_{\text{ion}} f_{\text{esc}}$, where ρ_{UV} is the integral of the UV luminosity function (Robertson et al. 2013). Observations indicate that the average galaxy population in reasonably complete samples down to $M_{\text{UV}} \approx -17$ at $z \gtrsim 6$ exhibits $\log(\xi_{\text{ion}}/\text{Hz erg}^{-1}) \approx 25.2 - 25.3$ (e.g., Mascia et al. 2024; Simmonds et al. 2024a; Pahl et al. 2025; Begley et al. 2026), consistent with, or only marginally higher than, pre-JWST canonical values (Robertson et al. 2015). For these ξ_{ion} , reionization models typically require population-averaged escape fractions of $f_{\text{esc}} \approx 10 - 20\%$ (Robertson et al. 2015), broadly supported by inferences using indirect LyC indicators (Mascia et al. 2023; Jaskot et al. 2024b; Jecmen et al. 2026) but with large scatter and sensitive to assumptions about the faint-end slope and cutoff of the UV luminosity function (e.g., Finkelstein et al. 2019; Korber et al. 2026). For simplicity, we adopt a fiducial scenario in which reionization is sustained by an averaged galaxy population characterized by $f_{\text{esc}} = 15\%$ and $\log(\xi_{\text{ion}}/\text{Hz erg}^{-1}) = 25.25$.

⁴ Given the widths of the NIRSpec/MSA and MIRI/LRS apertures of $\approx 0.2''$ and $0.5''$, respectively, within which no nebular emission appears detected. This corresponds to ~ 0.8 kpc and ~ 2.1 kpc at $z = 10.25$, i.e., much larger than the size of U37126 ($r_{\text{eff}} \approx 61$ pc).

We now consider a simple, illustrative scenario in which the ionizing budget is fully dominated by sources similar to U37126. Owing to their exceptionally high ξ_{ion} and near-unity f_{esc} , such systems could contribute disproportionately to \dot{n}_{ion} despite being rare. Requiring the ionizing emissivity contributed by these extreme sources to match that of the fiducial galaxy population yields:

$$\left(\frac{f_{\text{esc}}}{15\%}\right) \left(\frac{\xi_{\text{ion}}}{10^{25.25}}\right) = f_N \left(\frac{f_{\text{esc}}}{\geq 86\%}\right) \left(\frac{\xi_{\text{ion}}}{10^{25.75}}\right),$$

where f_N is the fraction of such extreme sources relative to the total galaxy population. Adopting the properties inferred for U37126, $\log(\xi_{\text{ion}}/\text{Hz erg}^{-1}) \simeq 25.75$ and $f_{\text{esc}} \geq 86\%$ (3σ ; Section 3), we find $f_N \lesssim 6\%$.

While this scenario is intentionally simplistic, implicitly assuming that such extreme values of ξ_{ion} and f_{esc} are independent of UV luminosity and populate the full luminosity function, it nevertheless illustrates that even a tiny fraction of powerful ionizing sources like U37126 could contribute significantly, or even dominate the ionizing photon budget during reionization.

In this regard, recent JWST observations are revealing a progressive steepening of UV slopes with increasing redshift (e.g., Topping et al. 2022; Cullen et al. 2024; Austin et al. 2025; Dottorini et al. 2025), with several sources at $z \gtrsim 6$ exhibiting extremely blue continua ($\beta_{\text{UV}} < -2.8$). As illustrated in Fig. 7, such UV slopes require very young stellar populations, implying elevated ionizing photon production efficiencies, $\xi_{\text{ion}} \gtrsim 10^{25.6} \text{ Hz erg}^{-1}$, together with high LyC escape fractions ($f_{\text{esc}} \gtrsim 50\%$; see Fig. 3). Moreover, the statistical analysis of Topping et al. (2024b) identified a small but non-negligible fraction ($\simeq 3.4\%$) of high-redshift sources with $\beta_{\text{UV}} < -2.8$ and indications of weak nebular emission, closely resembling U37126, which is comparable to the $f_N \lesssim 6\%$ of extreme LyC emitters required in our illustrative scenario. If spectroscopically confirmed, such systems could already account for a substantial fraction ($\gtrsim 50\%$) of the total ionizing photon budget during cosmic reionization.

5. Summary and Conclusions

In this work, we have presented very deep ($\simeq 11 \text{ h}$ on-source) JWST/MIRI LRS rest-frame optical spectroscopy of U37126, a $M_{\text{UV}} = -20.10$, mildly lensed ($\mu \sim 2.2$) galaxy at $z = 10.255$ previously identified with NIRSpec spectroscopy by Fujimoto et al. (2024).

The source exhibits an exceptionally steep UV continuum slope, $\beta_{\text{UV}} \simeq -2.9$, a weak Balmer break, a sharp Lyman- α break, and intrinsically faint nebular emission. Despite the clear detection of the continuum in both the NIRSpec/PRISM and MIRI/LRS spectra, no recombination or metal emission lines are detected. We derive stringent 3σ rest-frame equivalent-width upper limits of $\leq 64 \text{ \AA}$, $\leq 174 \text{ \AA}$, and $\leq 400 \text{ \AA}$ for $\text{H}\beta$, $[\text{O III}] \lambda 5008$, and $\text{H}\alpha$, respectively.

Combining these observational constraints with synthetic stellar population models, we have shown that the spectral properties of U37126 require both extremely young stellar ages and a very high Lyman-continuum escape fraction. Our results indicate ages $\leq 2 \text{ Myr}$ for instantaneous bursts or $\leq 10 \text{ Myr}$ for constant star formation, implying a very high ionizing photon production efficiency ($\log(\xi_{\text{ion}}/\text{Hz erg}^{-1}) \geq 25.6$). From the $\text{H}\alpha$ luminosity limit, we derive a conservative lower limit of $f_{\text{esc}} \geq 86\%$ (3σ), while independent SED fitting favors $f_{\text{esc}} = 0.94 \pm 0.06$.

U37126 is extremely compact, with a de-lensed effective radius of $r_{\text{eff}} \simeq 61 \text{ pc}$. The best-fit SED yields a (de-lensed) stellar mass of $M_{\star} \simeq 10^{7.8} M_{\odot}$ and a star-formation rate of $\text{SFR} \simeq 10 M_{\odot} \text{ yr}^{-1}$. This yields very high stellar mass and star-formation-rate surface densities of $\log(\Sigma_{M\star}/M_{\odot} \text{ pc}^{-2}) \simeq 3.4$ and $\log(\Sigma_{\text{SFR}}/M_{\odot} \text{ yr}^{-1} \text{ kpc}^{-2}) \simeq 2.6$, respectively, which are only comparable to those found in young massive star clusters and the most extreme sources at the highest redshifts.

Together with the lack of detectable nebular emission, these properties suggest that U37126 is undergoing an ISM-free starburst phase, in which the ISM is strongly depleted, and only a small fraction of ionizing photons are reprocessed by surrounding gas. Such conditions may result from both an extremely efficient gas-to-star conversion and/or strong feedback that has efficiently cleared the ISM from its stellar core.

Although systems like U37126 are likely rare, their extreme properties, combining both a high production and escape of LyC photons, suggest that they could contribute disproportionately to the ionizing photon budget during cosmic reionization. Even a small fraction of such sources ($\sim 3\%-6\%$) could account for a substantial share ($\sim 50\%-100\%$) of the required ionizing emissivity. This scenario is consistent with emerging JWST evidence for increasingly blue UV continua and weak nebular emission among the highest-redshift galaxies. If confirmed in larger statistical samples, these compact, highly efficient LyC emitters like U37126 may represent a key population responsible for driving and sustaining cosmic reionization.

Acknowledgements. J.A.-M., C.P.-J., B.R.P. acknowledge support by grant PID2024-158856NA-I00. J.A.-M., L.C., C.P.-J., B.R.P. acknowledge support by grant PIB2021-127718NB-100. P.G.P.-G. acknowledges support from grant PID2022-139567NB-I00 from the Spanish Ministry of Science and Innovation/State Agency of Research MCIN/AEI/10.13039/501100011033 and by “ERDF A way of making Europe”. J.A.-M., L.C., C.P.-J., B.R.P., P.G.P.-G. acknowledge support by grant CSIC/BILATERALES2025/BIJSP25022. M.C. acknowledges INAF GO Grant 2024 “Revealing the nature of bright galaxies at cosmic dawn with deep JWST spectroscopy”. T.H. was supported by JSPS KAKENHI 25K00020. Y.H. acknowledges support from the Japan Society for the Promotion of Science (JSPS) Grant-in-Aid for Scientific Research (24H00245), the JSPS Core-to-Core Program (JPJSCCA20210003), and the JSPS International Leading Research (22K21349). Y.F. is supported by JSPS KAKENHI Grant Numbers JP22K21349 and JP23K13149. D.L. was supported by research grants (VIL16599, VIL54489) from VILLUM FONDEN. The data were obtained from the Mikulski Archive for Space Telescopes at the Space Telescope Science Institute, which is operated by the Association of Universities for Research in Astronomy, Inc., under NASA contract NAS 5-03127 for JWST; and from the European JWST archive (eJWST) operated by the ESDC. This research made use of Photutils, an Astropy package for detection and photometry of astronomical sources (Bradley et al. 2022).

References

- Algera, H. S. B., Weaver, J. R., Bakx, T. J. L. C., et al. 2025, arXiv e-prints, arXiv:2512.14486
- Álvarez-Márquez, J., Colina, L., Crespo Gómez, A., et al. 2024, A&A, 686, A85
- Álvarez-Márquez, J., Crespo Gómez, A., Colina, L., et al. 2025, A&A, 695, A250
- Arrabal Haro, P., Dickinson, M., Finkelstein, S. L., et al. 2023, Nature, 622, 707
- Atek, H., Chemerynska, I., Wang, B., et al. 2023, MNRAS, 524, 5486
- Austin, D., Conselice, C. J., Adams, N. J., et al. 2025, ApJ, 995, 43
- Baker, W. M., D’Eugenio, F., Maiolino, R., et al. 2025, A&A, 697, A90
- Begley, R., McLure, R. J., Cullen, F., et al. 2026, MNRAS, 545, staf1995
- Bergvall, N., Leitet, E., Zackrisson, E., & Marquart, T. 2013, A&A, 554, A38
- Bezanson, R., Labbe, I., Whitaker, K. E., et al. 2024, ApJ, 974, 92
- Bhatawdekar, R. & Conselice, C. J. 2021, ApJ, 909, 144
- Boquien, M., Burgarella, D., Roehlly, Y., et al. 2019, A&A, 622, A103
- Bouwens, R. J., Illingworth, G. D., Oesch, P. A., et al. 2012, ApJ, 754, 83
- Bouwens, R. J., Illingworth, G. D., Oesch, P. A., et al. 2014, ApJ, 793, 115
- Bouwens, R. J., Illingworth, G. D., Oesch, P. A., et al. 2010, ApJ, 708, L69
- Boyett, K., Trenti, M., Leethochawalit, N., et al. 2024, Nature Astronomy, 8, 657
- Bradley, L., Sipócz, B., Robitaille, T., et al. 2022, astropy/photutils: 1.5.0

Bruzual, G. & Charlot, S. 2003, MNRAS, 344, 1000

Bunker, A. J., Saxena, A., Cameron, A. J., et al. 2023, A&A, 677, A88

Burgarella, D., Buat, V., & Iglesias-Páramo, J. 2005, MNRAS, 360, 1413

Burgarella, D., Buat, V., Theulé, P., et al. 2025, A&A, 699, A336

Bushouse, H., Eisenhamer, J., Dencheva, N., et al. 2025, JWST Calibration Pipeline

Calabro, A., Castellano, M., Zavala, J. A., et al. 2024, arXiv e-prints, arXiv:2403.12683

Calzetti, D., Armus, L., Bohlin, R. C., et al. 2000, ApJ, 533, 682

Calzetti, D., Kinney, A. L., & Storchi-Bergmann, T. 1994, ApJ, 429, 582

Cardelli, J. A., Clayton, G. C., & Mathis, J. S. 1989, ApJ, 345, 245

Carniani, S., Hainline, K., D'Eugenio, F., et al. 2024, Nature, 633, 318

Castellano, M., Fontana, A., Treu, T., et al. 2022, ApJ, 938, L15

Castellano, M., Napolitano, L., Fontana, A., et al. 2024, ApJ, 972, 143

Chabrier, G. 2003, PASP, 115, 763

Chemerynska, I., Atek, H., Furtak, L. J., et al. 2026, MNRAS[arXiv:2509.24881]

Chisholm, J., Saldana-Lopez, A., Flury, S., et al. 2022, MNRAS, 517, 5104

Crespo Gómez, A., Tamura, Y., Colina, L., et al. 2025, arXiv e-prints, arXiv:2511.14658

Cullen, F., McLeod, D. J., McLure, R. J., et al. 2024, MNRAS, 531, 997

Cullen, F., McLure, R. J., McLeod, D. J., et al. 2023, MNRAS, 520, 14

Curtis-Lake, E., Carniani, S., Cameron, A., et al. 2023, Nature Astronomy, 7, 622

de Barros, S., Vanzella, E., Amorín, R., et al. 2016, A&A, 585, A51

Dekel, A., Sarkar, K. C., Birnboim, Y., Mandelker, N., & Li, Z. 2023, MNRAS, 523, 3201

Dessauges-Zavadsky, M., Marques-Chaves, R., Schaefer, D., et al. 2025, A&A, 693, A17

Donnan, C. T., Dickinson, M., Taylor, A. J., et al. 2025, ApJ, 993, 224

Donnan, C. T., McLeod, D. J., McLure, R. J., et al. 2026, arXiv e-prints, arXiv:2601.11515

Dottorini, D., Calabro, A., Pentericci, L., et al. 2025, A&A, 698, A234

Ferrara, A., Giavalisco, M., Pentericci, L., et al. 2025, The Open Journal of Astrophysics, 8, 125

Ferrara, A., Pallottini, A., & Dayal, P. 2023, MNRAS, 522, 3986

Finkelstein, S. L., D'Aloisio, A., Paardekooper, J.-P., et al. 2019, ApJ, 879, 36

Finkelstein, S. L., Papovich, C., Salmon, B., et al. 2012, ApJ, 756, 164

Fiore, F., Ferrara, A., Bischetti, M., Feruglio, C., & Travascio, A. 2023, ApJ, 943, L27

Flury, S. R., Jaskot, A. E., Ferguson, H. C., et al. 2022, ApJ, 930, 126

Fujimoto, S., Wang, B., Weaver, J. R., et al. 2024, ApJ, 977, 250

Furtak, L. J., Zitrin, A., Weaver, J. R., et al. 2023, MNRAS, 523, 4568

Giovinozzi, E., Oesch, P. A., Weibel, A., et al. 2025, arXiv e-prints, arXiv:2507.01096

Goulding, A. D., Greene, J. E., Setton, D. J., et al. 2023, ApJ, 955, L24

Hainline, K. N., D'Eugenio, F., Jakobsen, P., et al. 2024, ApJ, 976, 160

Harikane, Y., Inoue, A. K., Ellis, R. S., et al. 2025, ApJ, 980, 138

Harikane, Y., Nakajima, K., Ouchi, M., et al. 2024, ApJ, 960, 56

Harikane, Y., Ouchi, M., Oguri, M., et al. 2023, ApJS, 265, 5

Harikane, Y., Perez-Gonzalez, P. G., Alvarez-Marquez, J., et al. 2026, arXiv e-prints, arXiv:2601.21833

Heintz, K. E., Watson, D., Brammer, G., et al. 2024, Science, 384, 890

Helton, J. M., Morrison, J. E., Hainline, K. N., et al. 2025, arXiv e-prints, arXiv:2512.19695

Hsiao, T. Y.-Y., Álvarez-Márquez, J., Coe, D., et al. 2024, ApJ, 973, 81

Inoue, A. K. 2010, MNRAS, 401, 1325

Isobe, Y., Ouchi, M., Nakajima, K., et al. 2023, ApJ, 956, 139

Izotov, Y. I., Schaefer, D., Thuan, T. X., et al. 2016, MNRAS, 461, 3683

Izotov, Y. I., Schaefer, D., Worseck, G., et al. 2025, A&A, 704, A19

Izotov, Y. I., Worseck, G., Schaefer, D., et al. 2018, MNRAS, 478, 4851

Jaskot, A. E., Silveyra, A. C., Plantinga, A., et al. 2024a, ApJ, 972, 92

Jaskot, A. E., Silveyra, A. C., Plantinga, A., et al. 2024b, ApJ, 973, 111

Jecmen, M. C., Chisholm, J., Atek, H., et al. 2026, arXiv e-prints, arXiv:2601.19995

Katz, H., Cameron, A. J., Saxena, A., et al. 2025, The Open Journal of Astrophysics, 8, 104

Kendrew, S., Scheithauer, S., Bouchet, P., et al. 2015, PASP, 127, 623

Kerutt, J., Oesch, P. A., Wisotzki, L., et al. 2024, A&A, 684, A42

Komarova, L., Oey, M. S., Marques-Chaves, R., et al. 2025, ApJ, 994, 192

Korber, D., Schaefer, D., Marques-Chaves, R., et al. 2026, arXiv e-prints, arXiv:2601.19989

Kuruvanthodi, A., Schaefer, D., Marques-Chaves, R., et al. 2024, A&A, 691, A310

Leitherer, C., Schaefer, D., Goldader, J. D., et al. 1999, ApJS, 123, 3

Li, Z., Dekel, A., Sarkar, K. C., et al. 2023, arXiv e-prints, arXiv:2311.14662

Looser, T. J., D'Eugenio, F., Maiolino, R., et al. 2024, Nature, 629, 53

Luridiana, V., Morisset, C., & Shaw, R. A. 2015, A&A, 573, A42

Marques-Chaves, R., Schaefer, D., Álvarez-Márquez, J., et al. 2021, MNRAS, 507, 524

Marques-Chaves, R., Schaefer, D., Álvarez-Márquez, J., et al. 2022, MNRAS, 517, 2972

Marques-Chaves, R., Schaefer, D., Dessauges-Zavadsky, M., et al. 2025, arXiv e-prints, arXiv:2510.12411

Marques-Chaves, R., Schaefer, D., Vanzella, E., et al. 2024, A&A, 691, A87

Mascia, S., Pentericci, L., Calabro, A., et al. 2024, A&A, 685, A3

Mascia, S., Pentericci, L., Calabro, A., et al. 2023, A&A, 672, A155

Menon, S. H., Burkhardt, B., Somerville, R. S., Thompson, T. A., & Sternberg, A. 2025, ApJ, 987, 12

Messa, M., Vanzella, E., Loiacono, F., et al. 2025, A&A, 694, A59

Morales, A. M., Finkelstein, S. L., Leung, G. C. K., et al. 2024, ApJ, 964, L24

Morishita, T., Stiavelli, M., Chary, R.-R., et al. 2024, ApJ, 963, 9

Naidu, R. P., Oesch, P. A., Brammer, G., et al. 2025, arXiv e-prints, arXiv:2505.11263

Naidu, R. P., Tacchella, S., Mason, C. A., et al. 2020, ApJ, 892, 109

Napolitano, L., Castellano, M., Pentericci, L., et al. 2025, A&A, 693, A50

Newville, M., Otten, R., Nelson, A., et al. 2025, LMFIT: Non-Linear Least-Squares Minimization and Curve-Fitting for Python

Osterbrock, D. E. & Ferland, G. J. 2006, Astrophysics of gaseous nebulae and active galactic nuclei

Pahl, A., Topping, M. W., Shapley, A., et al. 2025, ApJ, 981, 134

Pasha, I. & Miller, T. B. 2023, The Journal of Open Source Software, 8, 5703

Pérez-González, P. G., Costantin, L., Langeroodi, D., et al. 2023, ApJ, 951, L1

Perrin, M. D., Sivaramakrishnan, A., Lajoie, C.-P., et al. 2014, in Society of Photo-Optical Instrumentation Engineers (SPIE) Conference Series, Vol. 9143, Space Telescopes and Instrumentation 2014: Optical, Infrared, and Millimeter Wave, ed. J. Oschmann, Jacobus M., M. Clampin, G. G. Fazio, & H. A. MacEwen, 9143X

Planck Collaboration, Aghanim, N., Akrami, Y., et al. 2020, A&A, 641, A6

Price, S. H., Bezanson, R., Labbe, I., et al. 2025, ApJ, 982, 51

Reddy, N. A., Sanders, R. L., Shapley, A. E., et al. 2023a, ApJ, 951, 56

Reddy, N. A., Topping, M. W., Sanders, R. L., Shapley, A. E., & Brammer, G. 2023b, ApJ, 952, 167

Rieke, G. H., Wright, G. S., Böker, T., et al. 2015, PASP, 127, 584

Rivera-Thorsen, T. E., Dahle, H., Chisholm, J., et al. 2019, Science, 366, 738

Roberts-Borsani, G., Oesch, P., Ellis, R., et al. 2025, arXiv e-prints, arXiv:2508.21708

Robertson, B. E., Ellis, R. S., Furlanetto, S. R., & Dunlop, J. S. 2015, ApJ, 802, L19

Robertson, B. E., Furlanetto, S. R., Schneider, E., et al. 2013, ApJ, 768, 71

Saxena, A., Cameron, A. J., Katz, H., et al. 2024, arXiv e-prints, arXiv:2411.14532

Schaefer, D., Guibert, J., Marques-Chaves, R., & Martins, F. 2025, A&A, 693, A271

Sharma, M., Theuns, T., Frenk, C., et al. 2017, MNRAS, 468, 2176

Simmonds, C., Tacchella, S., Hainline, K., et al. 2024a, MNRAS, 527, 6139

Simmonds, C., Verhamme, A., Inoue, A. K., et al. 2024b, MNRAS, 530, 2133

Stanway, E. R. & Eldridge, J. J. 2018, MNRAS, 479, 75

Steidel, C. C., Bogosavljević, M., Shapley, A. E., et al. 2018, ApJ, 869, 123

Stiavelli, M., Morishita, T., Chiaberge, M., et al. 2023, ApJ, 957, L18

Suess, K. A., Weaver, J. R., Price, S. H., et al. 2024, ApJ, 976, 101

Tacchella, S., Eisenstein, D. J., Hainline, K., et al. 2023, ApJ, 952, 74

Tang, M., Stark, D. P., Mason, C. A., et al. 2025, arXiv e-prints, arXiv:2507.08245

Topping, M. W., Stark, D. P., Endsley, R., et al. 2022, ApJ, 941, 153

Topping, M. W., Stark, D. P., Endsley, R., et al. 2024a, MNRAS, 529, 4087

Topping, M. W., Stark, D. P., Senchyna, P., et al. 2024b, MNRAS, 529, 3301

Vanzella, E., Claeysens, A., Welch, B., et al. 2023, ApJ, 945, 53

Vanzella, E., de Barros, S., Vasei, K., et al. 2016, ApJ, 825, 41

Weaver, J. R., Cutler, S. E., Pan, R., et al. 2024, ApJS, 270, 7

Weibel, A., Oesch, P. A., Barrufet, L., et al. 2024, MNRAS, 533, 1808

Wright, G. S., Rieke, G. H., Glasse, A., et al. 2023, PASP, 135, 048003

Wright, G. S., Wright, D., Goodson, G. B., et al. 2015, PASP, 127, 595

Yanagisawa, H., Ouchi, M., Nakajima, K., et al. 2025, ApJ, 988, 86

Zackrisson, E., Binggeli, C., Finlator, K., et al. 2017, ApJ, 836, 78

Zackrisson, E., Inoue, A. K., & Jensen, H. 2013, ApJ, 777, 39

Zavala, J. A., Castellano, M., Akins, H. B., et al. 2025, Nature Astronomy, 9, 155

¹ Geneva Observatory, Department of Astronomy, University of Geneva, Chemin Pegasi 51, CH-1290 Versoix, Switzerland

² Centro de Astrobiología (CAB), CSIC-INTA, Ctra. de Ajalvir km 4, Torrejón de Ardoz, E-28850, Madrid, Spain

³ European Space Agency (ESA), ESA Office, Space Telescope Science Institute, 3700 San Martin Drive, Baltimore, MD 21218, USA

⁴ Department of Astronomy, Indiana University, 727 East Third Street, Bloomington, IN 47405, USA

- ⁵ Leiden Observatory, Leiden University, PO Box 9513, NL-2300 RA Leiden, The Netherlands
- ⁶ INAF – Osservatorio Astronomico di Roma, via Frascati 33, 00078, Monteporzio Catone, Italy
- ⁷ Kapteyn Astronomical Institute, University of Groningen, P.O. Box 800, 9700AV Groningen, The Netherlands
- ⁸ Space Telescope Science Institute (STScI), 3700 San martin Drive, Baltimore, MD 21218, USA
- ⁹ Center for Frontier Science, Chiba University, 1-33 Yayoi-cho, Inage-ku, Chiba 263-8522, Japan
- ¹⁰ David A. Dunlap Department of Astronomy and Astrophysics, University of Toronto, 50 St. George Street, Toronto, Ontario, M5S 3H4, Canada
- ¹¹ Dunlap Institute for Astronomy and Astrophysics, 50 St. George Street, Toronto, Ontario, M5S 3H4, Canada
- ¹² Institute for Cosmic Ray Research, The University of Tokyo, 5-1-5 Kashiwanoha, Kashiwa, Chiba 277-8582, Japan
- ¹³ Division of Physics, Faculty of Pure and Applied Sciences, University of Tsukuba, Tsukuba, Ibaraki 305-8571, Japan
- ¹⁴ Tomonaga Center for the History of the Universe (TCHoU), Faculty of Pure and Applied Sciences, University of Tsukuba, Tsukuba, Ibaraki 305-8571, Japan
- ¹⁵ Department of Astronomy, University of Texas, Austin, TX 78712, USA
- ¹⁶ Institute of Science and Technology Austria (ISTA), Am Campus 1, 3400 Klosterneuburg, Austria
- ¹⁷ Department of Physics, School of Advanced Science and Engineering, Faculty of Science and Engineering, Waseda University, 3-4-1 Okubo, Shinjuku, Tokyo 169-8555, Japan
- ¹⁸ Waseda Research Institute for Science and Engineering, Faculty of Science and Engineering, Waseda University, 3-4-1 Okubo, Shinjuku, Tokyo 169-8555, Japan
- ¹⁹ DARK, Niels Bohr Institute, University of Copenhagen, Jagtvej 155A, 2200 Copenhagen, Denmark
- ²⁰ University of Massachusetts Amherst, 710 North Pleasant Street, Amherst, MA 01003-9305, USA
- ²¹ Department of Astronomy, Stockholm University, Oscar Klein Centre, AlbaNova University Centre, 106 91 Stockholm, Sweden
- ²² AURA for the European Space Agency (ESA), Space Telescope Science Institute, 3700 San Martin Dr., Baltimore, MD 21218, USA
- ²³ UK Astronomy Technology Centre, Royal Observatory Edinburgh, Blackford Hill, Edinburgh EH9 3HJ, UK

Appendix A: BPASS predictions for different metallicities

Figure A.1 shows the model predictions of the UV slope, $EW_0(\text{H}\alpha)$ and the Balmer break strength as a function of age for different stellar metallicities (from solar to $Z/Z_\odot = 0.05$) and different LyC escape fractions ($f_{\text{esc}} = 0\%, 50\%, \text{ and } 90\%$).

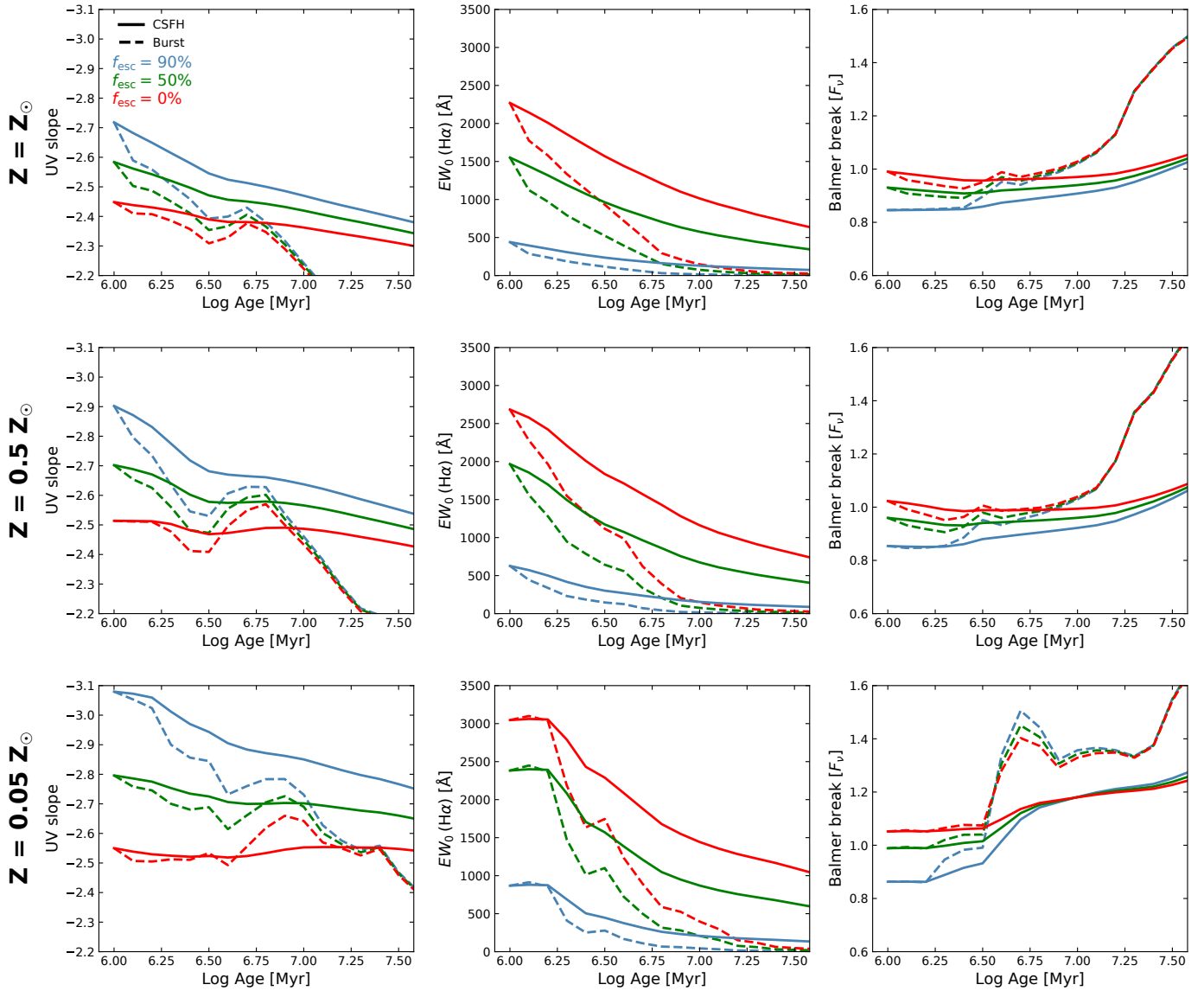


Fig. A.1. Stellar+nebular predictions of the UV slope (left), $EW_0(\text{H}\alpha)$ (middle) and the Balmer break strength (right) as a function of age for different stellar metallicities, from solar (top) to $Z/Z_{\odot} = 0.05$ (bottom). Nebular emission is assumed with $T_e = 1.5 \times 10^4$ K and $n_e = 10^3 \text{ cm}^{-3}$. Solid and dashed lines correspond to constant star formation and instantaneous burst models, respectively. Model sequences are shown for LyC escape fractions $f_{\text{esc}} = 0\%$ (red), 50% (green), and 90% (blue).